PTEP

Prog. Theor. Exp. Phys. **2021**, 103D04 (11 pages)
DOI: 10.1093/ptep/ptab115

Ξ hypernuclear states predicted by next-to-leading-order chiral baryon–baryon interactions

M. Kohno[1,*] and K. Miyagawa[1,2]

[1]*Research Center for Nuclear Physics, Osaka University, Ibaraki 567-0047, Japan*
[2]*Graduate School of Science, Okayama University of Science, Okayama 700-0005, Japan*
*E-mail: kohno@rcnp.osaka-u.ac.jp

Received July 5, 2021; Revised August 12, 2021; Accepted August 27, 2021; Published September 4, 2021

The Ξ single-particle potential obtained in nuclear matter with next-to-leading-order baryon–baryon interactions in chiral effective field theory is applied to finite nuclei by an improved local-density approximation method. As a premise, phase shifts of ΞN elastic scattering and the results of Faddeev calculations for the ΞNN bound state problem are presented to show the properties of the ΞN interactions in the present parametrization. First, the Ξ states in ^{14}N are revisited because of recent experimental progress, including discussion on the ΞN spin–orbit interaction that is relevant to the location of the p-state. Then the Ξ levels in ^{56}Fe are calculated. In particular, the level shift which is expected to be measured experimentally in the near future is predicted. The smallness of the imaginary part of the Ξ single-particle potential is explicitly demonstrated.

Subject Index D14

1. Introduction

New experimental information on the Ξ–nucleus interaction is increasing from analyses of experiments at J-PARC. The first observation of twin single-Λ hypernuclei in an experiment at J-PARC identified a Ξ^-–^{14}N bound state with the binding energy $B_\Xi = 1.27 \pm 0.21$ MeV [1]. This energy is close to the candidate of the Ξ^-–^{14}N state observed in the previous KEK E373 experiment [2] with $B_\Xi = 1.03 \pm 0.18$ MeV. In the near future, further observations of Ξ bound states in nuclei are expected. Inclusive spectra of (K^-, K^+) reactions on nuclei [3] should provide the properties of the Ξ–nucleus potential in a wide energy range. Another ongoing experiment to detect Ξ atomic level shifts by measuring electromagnetic transition spectra [4] is also valuable for information on the Ξ–nucleus potential in the surface region.

On the theoretical side, construction of baryon–baryon interactions in the strangeness $S = -2$ sector has been developed in the framework of chiral effective field theory (ChEFT) [5–7]. The $S = -2$ sector of octet baryon–baryon interactions is the middle of the possible strangeness contents from $S = 0$ to -4 and therefore all the combinations of the flavor SU(3) bases participate in the interaction features. The lattice quantumchromodynamics (QCD) method by the HAL-QCD group has also provided the parametrization of the $S = -2$ interactions [8,9]. Both descriptions are based on QCD, namely the underlying theory of hadrons and their interactions, either in a direct way or by way of low-energy chiral effective field theory. The ΞN interactions of these two methods are, interestingly, similar even at the quantitative level, as shown in the following section. An attempt

[10] has also been made to determine some low-energy constants in the relativistic ChEFT at leading order by fitting them to the HAL-QCD data in the $S = -2$ sector.

Because it is not feasible in the near future to directly measure Ξ–nucleon scattering, information on the Ξ bound states is the chief source for the ΞN interactions. It is hard, however, to find the detailed spin and isospin structure of the ΞN interaction from analysis of the bound state data in itself. It is necessary to compare the experimental data with the results of microscopic calculations using theoretical interactions that are as reliable as possible.

In Ref. [11], one of the present authors reported the properties of the Ξ–nucleus single-particle potential which are obtained on the basis of G-matrix calculations in symmetric nuclear matter with next-to-leading order (NLO) ChEFT potentials with a cutoff scale of $\Lambda_c = 550$ MeV constructed by the Jülich–Bonn–München group [6,7]. There, Ξ potentials in light nuclei such as ^{9}Be, ^{12}C, and ^{14}N are predicted through the translation of the potential in infinite matter to that in a finite nucleus by an improved local-density approximation (ILDA) method. In view of the current experimental efforts, it is meaningful to revisit the case of ^{14}N and extend the calculation of the chiral Ξ potential to heavy nuclei such as ^{56}Fe.

In Sect. 2, the basic properties of chiral NLO ΞN interactions are elucidated by presenting ΞN phase shifts, and the results of the Faddeev calculations for searching a ΞNN bound state. The Ξ^- single-particle potentials in heavier nuclei are studied in Sect. 3. First, the Ξ^- states predicted on ^{14}N are revisited. The probable $0p$ Ξ^- state observed experimentally [1] is conducive to the discussion of the Ξ spin–orbit single-particle potential. Next, the potential for ^{56}Fe is presented, for which the measurement of the level shift of a certain atomic level is aimed in the J-PARC experiment. The very small imaginary part of the Ξ single-particle potential is demonstrated. A summary follows in Sect. 4.

2. Properties of chiral NLO ΞN interaction

2.1. ΞN phase shift

It is basic to evaluate phase shifts of elastic scattering to elucidate the properties of the ΞN interaction in each spin and isospin channel. The s-wave phase shifts calculated with an updated version of the chiral NLO interactions with $\Lambda_c = 550$ MeV [7] are shown in Fig. 1 with solid curves. The calculations are in the isospin base; that is, the average masses are assigned for the N, Σ, and Ξ baryons, respectively. The phase shifts with the interactions parametrized on the basis of HAL-QCD calculations are also included for comparison. There are two sets of parametrization based on the same HAL-QCD calculations. The dashed curves represent the results of the potential by Inoue et al. [8] in which the baryon-channel coupling components are explicitly parametrized as a local function. The dotted curves are the results of the potential of the fit for $t/a = 12$ by Sasaki et al. [9] in which the effects of the tensor coupling and the baryon-channel coupling except for ΛΛ are simulated by a local ΞN potential in coordinate space.

It can be seen that three potentials predict qualitatively similar behavior of the phase shifts in all spin and isospin states. The interaction in the isospin $T = 1$ and $^1S_0$ state is repulsive, and the interactions in the remaining three states are attractive. Nevertheless, some quantitative differences are remarked. The repulsion of the $T = 1$ ^{1}S$_0$ part of the Sasaki potential is very weak. The attraction in the $T = 1$ ^{3}S$_1$ state of the HAL-QCD parametrization is smaller than that of ChEFT. The attraction in the $T = 0$ $^3S_1$ state, in which no baryon-channel coupling is present, is weak. The $T = 0$ $^1S_0$ state is most attractive, although no bound state exists. This attraction originates from the

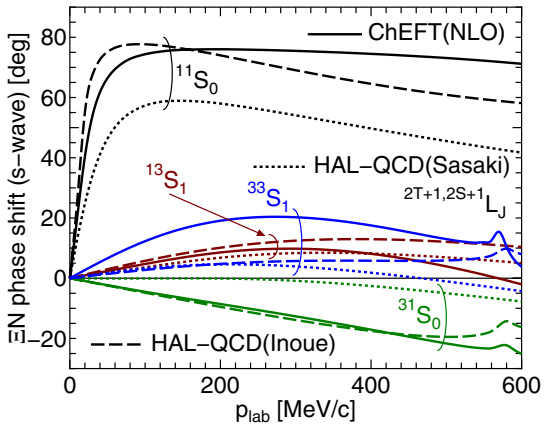

Fig. 1. ΞN s-wave phase shifts calculated with NLO ChEFT interactions ($\Lambda_c = 550$ MeV) [7] are shown by solid curves with the notation ${}^{2T+1,2S+1}L_J$ specifying the spin S and isospin T channel. Phase shifts with two sets of parametrization based on the HAL-QCD calculations are also shown: one is the full parametrization from Ref. [8] (dashed) and the other is the fit for $t/a = 12$ from Ref. [9] (dotted).

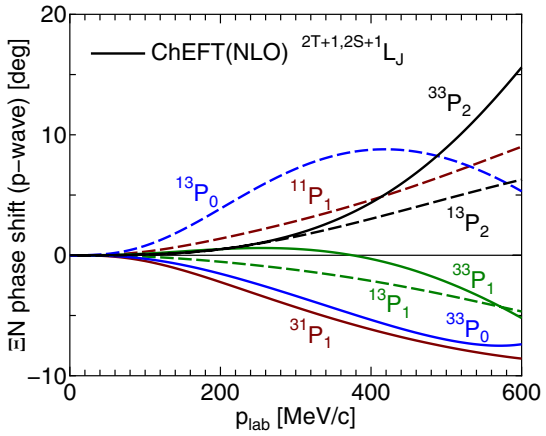

Fig. 2. ΞN p-wave phase shifts calculated with NLO ChEFT interactions ($\Lambda_c = 550$ MeV) [7]. Those of the isospin $T = 0$ ($T = 1$) states are denoted by dashed (solid) curves.

coupling to the $\Lambda\Lambda$ as well as $\Sigma\Sigma$ states, though the effect of the ΞN–$\Lambda\Lambda$ coupling is smaller than that of the ΞN–$\Sigma\Sigma$ coupling in the HAL-QCD potentials. The attractive character in the $T = 1$ ${}^3S_1$ state is not so prominent as in the $T = 0$ ${}^1S_0$ state but plays an important role in generating an attractive Ξ single-particle potential in a nucleus because of the spin–isospin weight factor of $(2S + 1)(2T + 1) = 9$.

The uncertainties in the ChEFT parametrization of p-waves are larger than those in the s-waves [6]. The antisymmetric spin–orbit interactions, which couple the spin-single and triplet states with the same total spin J, are absent in the present chiral NLO interactions [6]. Still, it is meaningful to present p-wave phase shifts for inferring the effects of the p-waves on the Ξ–nucleus potential. The p-wave phase shifts calculated with the chiral NLO interactions [6] are shown in Fig. 2. The phase shifts are rather small, except for in the $T = 1$ ${}^3P_2$ state, the attraction of which grows with increasing energy. The corresponding attractive contribution to the Ξ single-particle potential in symmetric nuclear matter was presented in Fig. 2 of Ref. [11]. It is also seen in that figure that the

contributions to the Ξ single-particle potential from other p-states are small and tend to cancel each other.

2.2. ΞNN three-body system

It is important to figure out whether the chiral NLO interaction can support a ΞNN three-body bound state. The results of the Faddeev calculation for the ΞNN bound state problem are recapitulated in this section. In the present calculations, two-body ΞN T-matrices are first prepared by solving a baryon-channel coupled Lippmann–Schwinger equation in momentum space. In the isospin $T = 0$ case, the ΞN–$\Lambda\Lambda$–$\Sigma\Sigma$ coupling is present in the $^1S_0$ state, while no baryon-channel coupling exists in the $^3S_1$–$^3D_1$ tensor correlated state. In the $T = 1$ case, the ΞN–$\Lambda\Sigma$ coupling is present in the $^1S_0$ state, and the ΞN–$\Lambda\Sigma$–$\Sigma\Sigma$ coupling takes place in the $^3S_1$–$^3D_1$ tensor correlated state. Then, the evaluated T-matrices are used in the Faddeev equation for the ΞNN bound-state problem:

$$\Psi^{(23)} = G_0 T_{NN}(1 - P_{23})\Psi^{(12)}, \tag{1}$$

$$\Psi^{(12)} = G_0 T_{\Xi N}(\Psi^{(23)} - P_{23}\Psi^{(12)}), \tag{2}$$

where G_0 is a three-particle propagator, $\Psi^{(ij)}$ is the Faddeev component, and P_{23} is the transposition operator for the 2–3 pair, assigning the number 1 to Ξ and the remaining 2 and 3 to the nucleons. This procedure means that while the pairwise correlation is fully solved, the entire three-baryon coupling is not considered. The interactions are also restricted to the s-wave except for the tensor-coupled d-wave. The Coulomb force is also not taken into account. Still, the calculation is an important attempt at a realistic description of the ΞNN system.

In the literature, possible ΞNN bound states have been reported [12,13] using the s-wave single-channel ΞN potential simulating the Nijmegen ESC08c model [14] for the ΞN interaction and the central s-wave Malfliet–Tjon NN potential [16] for the NN interaction. The Faddeev calculations in Ref. [13] without the Coulomb force show that the bound state exists at a binding energy of $B = 17.2$ MeV in the spin–isospin $(S, T) = (3/2, 1/2)$ state and $B = 2.9$ MeV in the $(S, T) = (1/2, 3/2)$ state. These results are reproduced in our momentum-space Faddeev calculations.

The situation is different when the chiral NLO $S = -2$ interactions are used together with the N^{3}LO NN interactions [17]. The results of our Faddeev calculations show that no hypernuclear bound ΞNN system is expected in every possible spin–isospin channel. It is also ascertained that even if the repulsive $T = 1$ $^1S_0$ ΞN interaction is omitted, the ΞNN system is not bound. The details are reported in Ref. [18]. Qualitative differences exist between the ESC08c and the NLO ChEFT ΞN s-wave interactions. The attraction in the $T = 1$ $^3S_1$ channel of ESC08c is attractive enough to provide a ΞN bound state, and the $T = 0$ $^1S_0$ interaction of ESC08c is repulsive, contrary to that of NLO ChEFT. It is noted, however, that a substantial revision was made for ESC08c to construct the new version as ESC16 [15].

3. Ξ bound states in finite nuclei

Although the ΞNN system is not bound with the present NLO chiral interactions, the Ξ hyperon can be bound in heavier nuclei due to the attraction in the $T = 1$ $^3S_1$ channel with the statistical factor of $(2S + 1)(2T + 1)$. As shown in Ref. [11], the Ξ^- single-particle potentials predicted for ^{9}Be, ^{12}C, and ^{14}N by the ILDA method using the G-matrices in symmetric nuclear matter with the NLO chiral interactions are rather shallow, but attractive enough to support hypernuclear bound states. In this section, the calculated Ξ^-–^{14}N bound states are first revisited concerning the recent experimental

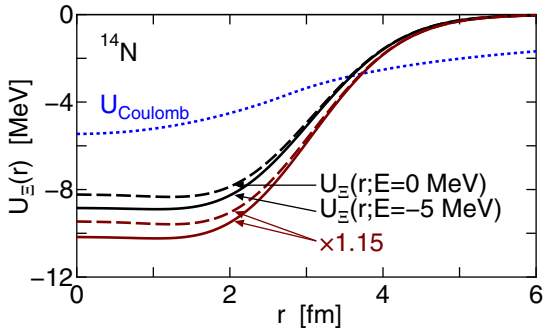

Fig. 3. Energy-dependent Ξ–^{14}N single-particle potential by the ILDA method, using ΞN G-matrices in symmetric nuclear matter with the NLO ChEFT interactions [7]. The potentials enhanced by a factor of 1.15 are also shown. $U_{\rm Coulomb}$ is the potential of a uniform charge distribution with a radius of $R_{\rm C} = 1.15A^{1/3}$ fm.

data and the possible effect of the Ξ spin–orbit potential for the p-state. Next, Ξ^- bound states in ^{56}Fe are presented. In particular, the atomic level shift of Ξ^- in ^{56}Fe is focused on, for which the X-ray spectroscopy experiment to detect it is ongoing at J-PARC [4]. The very small imaginary part of the Ξ potential is shown, which was not included in Ref. [11].

3.1. Ξ^-–^{14}N bound states and Ξ spin–orbit potential

After the prediction for Ξ^- bound states in ^{14}N was reported in Ref. [11] based on the NLO ChEFT $S = -2$ interactions, new experimental information [1] was obtained through the first observation of twin single-Λ hypernuclei: $\Xi^- + ^{14}\mathrm{N} \to ^{10}_{\Lambda}\mathrm{Be} + ^{5}_{\Lambda}\mathrm{He}$. The state is probably a $0p$ level at 1.27 ± 0.21 MeV. Further observation of Ξ^- states in ^{14}N was also reported [19] from the analyses of the data of KEK and J-PARC experiments. That is, three candidates for the $0s$ state are at 8.00 ± 0.77, 4.96 ± 0.77, and 6.27 ± 0.27 MeV, respectively, and a possible $0p$ state is at 0.90 ± 0.62 MeV. These energies are shown on the left side of Fig. 4.

Observing that the calculated energies in Ref. [11] correspond reasonably well to these experimental data, additional calculations are given in this subsection. First, if the experimental energy of 6.27 ± 0.27 MeV is taken seriously, the calculated Ξ^- $0s$ energy of -5.40 MeV in Table II of Ref. [11] is slightly short. To reproduce the range of the empirical energy, -6.00––6.54 MeV, it is necessary to multiply by a factor of 1.10–1.19 the calculated Ξ–^{14}N potential. This factor appears within the uncertainties of the G-matrix calculations and the ILDA method. The calculated Ξ–^{14}N single-particle potential is shown in Fig. 3. The potential by the ILDA method is energy dependent. $U_\Xi(r; E = -5\,\mathrm{MeV})$ is employed for the $0s$ state, and $U_\Xi(r; E = 0\,\mathrm{MeV})$ for the $0p$ and $0d$ states. The evaluated single-particle energies are presented in Fig. 4 for both U_Ξ and $1.15 \times U_\Xi$. The position of the $0p$ level is reasonable. It is noted that the Coulomb $0d$ state is hardly affected by the addition of the hypernuclear potential $U_\Xi(r; E = 0\,\mathrm{MeV})$.

Another subject to discuss here is the effect of a Ξ-nucleus spin–orbit potential. If the Ξ spin–orbit interaction is not negligible, the location of the $0p$ state does not simply imply the strength of the Ξ central single-particle potential. Although the ground state of ^{14}N is not simply shell-closed, it is instructive to estimate how the Ξ $0p$ level in ^{14}N is affected by the possible spin–orbit potential in a mean-field consideration; that is, without considering the detailed structure of the ^{14}N ground state.

The interesting feature of the Ξ spin–orbit single-particle potential in nuclei is that the potential may be repulsive in contrast to the attractive nucleon spin–orbit potential. Various theoretical studies have predicted a repulsive Ξ spin–orbit mean field, though the strength is considerably smaller than

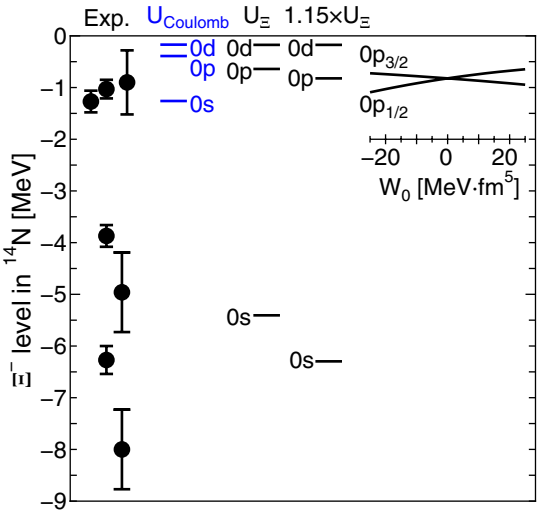

Fig. 4. Ξ^- single-particle states in ^{14}N. Experimental data on the left side are taken from the compilation in Ref. [19]. The Coulomb attraction is treated by the potential of uniform charge distribution with a radius of $R_C = 1.15A^{1/3}$ fm. The ILDA potential is energy dependent. $U_\Xi(r; E = -5\,\text{MeV})$ is employed for the $0s$ state and $U_\Xi(r; E = 0\,\text{MeV})$ for the $0p$ and $0d$ states. It is demonstrated that an enhancement factor of 1.15 is needed to fit the $0s$ energy at 6.27 MeV. The shifts of the $0p_{3/2}$ and $0p_{1/2}$ energies due to the addition of the ΞN spin–orbit potential is shown on the right side, as a function of the strength W_0 from Eq. (5).

that of the nucleon. When the spin–orbit potential is repulsive, the downward shift of the single-particle level with $j_< = \ell - \frac{1}{2}$ is twice as large as that of the level with $j_> = \ell + \frac{1}{2}$ for the attractive one.

In a relativistic mean-field description [20–22], the repulsive spin–orbit mean field is brought about by an ω-meson exchange with the tensor coupling. The repulsive character is also predicted in a microscopic description based on two-body ΞN interactions constructed in a non-relativistic SU(6) quark model [23], in which the contribution from the ordinary spin–orbit component of the ΞN interaction is attractive, while the antisymmetric spin–orbit component has an opposite contribution and the net spin–orbit single-particle potential becomes repulsive. In all these estimations, the repulsive strength is one-fifth of the attractive strength of the nucleon spin–orbit potential or less.

The effective spin–orbit strength generated by the bare baryon–baryon interaction is properly measured by the Scheerbaum factor [24] calculated in nuclear matter. The expression for the nucleon case was extended to the hyperon cases in Ref. [23]. The Scheerbaum factor for Ξ in symmetric nuclear matter with the Fermi momentum k_F reads

$$S_\Xi(\bar{q}) = \frac{\zeta(1+\zeta)^2}{8k_F^3} \sum_{JT} (2J+1)(2T+1) \int_0^{q_{\max}} dq\; W(\bar{q},q) \times \{(J+2)G^{JT}_{1J+1,1J+1}(q) + G^{JT}_{1J,1J}(q) - (J-1)G^{JT}_{1J-1,1J-1}(q)\}. \tag{3}$$

Here, $\zeta \equiv m_N/m_\Xi$, $q_{\max} = \frac{1}{2}(k_F + \bar{q})$, and the weight factor $W(\bar{q},q)$ is defined by

$$W(\bar{q},q) = \begin{cases} \theta(k_F - \bar{q}) & \text{for } 0 \le q \le \frac{|k_F - \bar{q}|}{2}, \\ \frac{k_F^2 - (\bar{q}-2q)^2}{8\bar{q}q} & \text{for } \frac{|k_F-\bar{q}|}{2} \le q \le \frac{k_F+\bar{q}}{2}, \end{cases} \tag{4}$$

where $\theta(k_F - \bar{q})$ is a step function. In Eq. (3), $G^{JT}_{1\ell',1\ell}$ is the abbreviation of the momentum-space diagonal G-matrix element in the spin-triplet channel with the total spin J and total isospin T.

The above definition of S_Ξ is different from the original constant in Ref. [24] by a factor of $-\frac{2\pi}{3}$. Then, S_Ξ can be identified with the strength W_0 of the δ-type effective two-body spin–orbit interaction customarily used in Skyrme–Hartree–Fock calculations [25]:

$$iW_0(\boldsymbol{\sigma}_1 + \boldsymbol{\sigma}_2) \cdot [\nabla_r \times \delta(\boldsymbol{r})\nabla_r]. \tag{5}$$

In the present NLO ChEFT interaction, the antisymmetric spin–orbit term is not included by putting the pertinent low-energy constant to zero. Therefore, the spin–orbit interaction in the nuclear medium is expected to be attractive. The actual G-matrix calculation in symmetric nuclear matter gives $S_\Xi \simeq 21.5\,\mathrm{MeV{\cdot}fm^5}$ at $\bar{q} \approx 0.7\,\mathrm{fm}^{-1}$, the value prescribed by Scheerbaum on the basis of the wavelength of the density distribution. This value is about one-fifth of $S_N = 102\,\mathrm{MeV{\cdot}fm^5}$ with the same sign [26,27]. It is noted that $S_N = 102\,\mathrm{MeV{\cdot}fm^5}$ is somewhat smaller than the typical value of $S_N = 120\,\mathrm{MeV{\cdot}fm^5}$ used in Skyrme–Hartree–Fock calculations in the literature.

Changes of the Ξ^- $0p$ level in ^{14}N of the potential $1.15 \times U_\Xi(E = 0\,MeV)$ depending on the spin–orbit parameter W_0 from -25 to $25\,\mathrm{MeV{\cdot}fm^5}$ are depicted in Fig. 4. The negative sign of W_0 means a repulsive spin–orbit potential. If the spin–orbit potential strength is about one-fifth that of the nucleon, the energy splitting of the shallow $0p_{1/2}$ and $0p_{3/2}$ states in ^{14}N is about 0.4 MeV.

3.2. Ξ bound states in ^{56}Fe and atomic level shifts

In applying the ILDA method [11] to generate the Ξ single-particle potential in ^{56}Fe using G-matrices evaluated in symmetric nuclear matter, one has to beware that the ^{56}Fe nucleus is asymmetric in the proton and neutron density distributions. At present, however, it is very demanding to perform Brueckner self-consistent calculations of the Ξ potential at various asymmetric nuclear matter, because all single-particle potentials of the eight octet baryons (n, p, Λ, Σ^-, Σ^0, Σ^+, Ξ^-, and Ξ^0) have to be determined self-consistently. Fortunately, the asymmetric effect can be expected to be small, as explained in the following. If the neutron and proton contributions are individually written, the Ξ potential is obtained by the sum of the proton and neutron contributions, which is written in an abbreviated notation as

$$U_{\Xi^-} = \rho_n G^3 + \frac{1}{2}\rho_p(G^1 + G^3), \tag{6}$$

where ρ_n and ρ_p are the neutron and proton density distributions, respectively, and G^{2T+1} represents the contribution of the ΞN G-matrix in the isospin T channel. Introducing the asymmetry parameter α as $\alpha \equiv (\rho_n - \rho_p)/(\rho_n + \rho_p) \equiv (\rho_n - \rho_p)/\rho$, the potential U_{Ξ^-} is written as

$$U_{\Xi^-} = \frac{1}{4}\rho(G^1 + 3G^3)\left\{1 + \alpha\frac{G^3 - G^1}{3G^3 + G^1}\right\}. \tag{7}$$

The profile of the neutron and proton density distributions of the density-dependent Hartree–Fock calculation with the G-0 force of Ref. [28], which is used in the present ILDA calculations of the Ξ potential in ^{56}Fe, is shown in Fig. 5. The asymmetry of ^{56}Fe is seen to be about $\alpha \approx \frac{0.01}{0.15} = \frac{1}{15}$. The additional factor $(G^3 - G^1)/(3G^3 + G^1)$ is smaller than $\frac{1}{3}$, as inferred from the properties of the ΞN interaction presented in Sect. 2. Therefore, the contribution of the second term in Eq. (7) is estimated to be at most 2% of the first term. This indicates that the estimation of the Ξ^- potential based on G-matrices in symmetric nuclear matter is reliable.

The Ξ–^{56}Fe single-particle potential calculated by the ILDA method with the Gaussian smearing range of $\beta = 1.0$ fm is shown in Fig. 6. The solid and dashed curves represent the real and imaginary

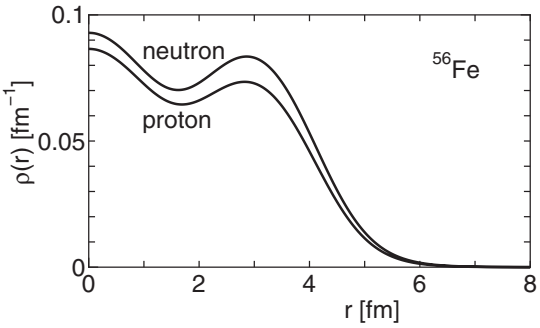

Fig. 5. Point proton and neutron density distributions $\rho(r)$ of ^{56}Fe obtained by density-dependent Hartree–Fock calculations with the G0 force of Ref. [28].

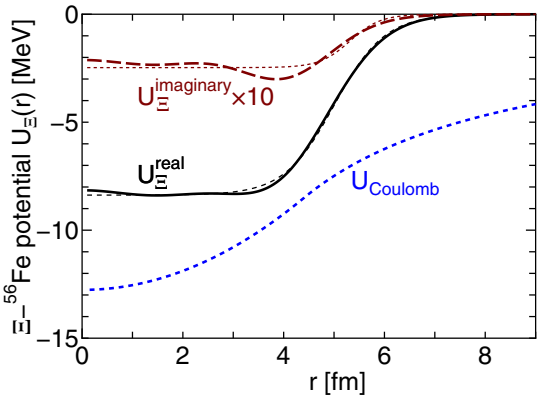

Fig. 6. Ξ single-particle potential obtained in the ILDA method, based on the Ξ potential in symmetric nuclear matter calculated with the NLO ChEFT interactions [6]. The imaginary part shown by the dashed curve is scaled up by a factor of 10. The dotted curves are the potential fitted in a Woods–Saxon form; the depth and the geometry parameters are given in the text. $U_{\rm Coulomb}$ depicts the Coulomb potential of the uniform charge distribution with radius $R_{\rm C} = 1.15A^{1/3}$ fm.

parts, respectively. The potential in symmetric nuclear matter is energy dependent. The energy is set to be 0 MeV because the shallow Ξ level is mainly concerned to discuss the Coulomb energy level shift. The potential shape is well simulated by a standard Woods–Saxon form in both the real and imaginary parts. The fitted strength and geometry parameters are $V_{\rm R} = -8.39$ MeV, $R_{0,\rm R} = 5.01$ fm, and $a_{\rm R} = 0.499$ fm for the real part, and $V_{\rm I} = -0.247$ MeV, $R_{0,\rm I} = 5.32$ fm, and $a_{\rm I} = 0.303$ fm for the imaginary part. These Woods–Saxon potentials are shown by the dotted curves in Fig. 6.

The depth of the real part of about 8 MeV corresponds to that in nuclear matter. The imaginary potential, which mainly originates from the energy-conserving $\Xi N \to \Lambda\Lambda$ process, turns out to be very small. Note that the imaginary part is scaled up by a factor of 10 in Fig. 6. In this transition process, the kaon exchange has to be involved and therefore the interaction is short-ranged. The smallness of the ΞN–$\Lambda\Lambda$ coupling potential is also pointed out in the HAL-QCD calculations [9].

To see more details of the features of the ΞN–$\Lambda\Lambda$–$\Sigma\Sigma$ coupling, it is instructive to calculate ΞN phase shifts in the $T = 0$ ^{1}S$_0$ channel switching off the baryon-channel coupling. Figure 7 represents these phase shifts of NLO ChEFT in the left panel and of HAL-QCD in the right panel. The coupling effect appears rather small in both the $\Lambda\Lambda$ and $\Sigma\Sigma$ channels in NLO ChEFT, but these two channels contribute constructively. In the HAL-QCD parametrization of Ref. [8], the contribution of the $\Lambda\Lambda$

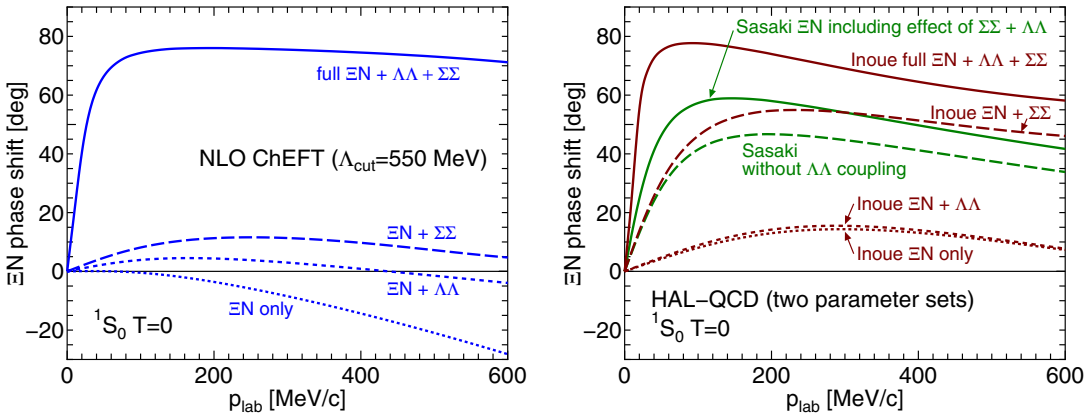

Fig. 7. $T = 0$ ^{1}S$_0$ ΞN phase shifts calculated by switching off the $\Lambda\Lambda$ and/or $\Sigma\Sigma$ coupling: NLO ChEFT [7] in the left panel and HAL-QCD [8,9] in the right panel.

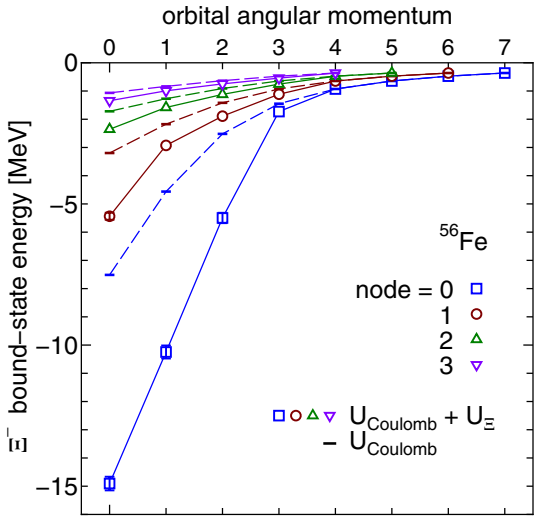

Fig. 8. Ξ single-particle levels in ^{56}Fe obtained by the potential $U_{\rm Coulomb} + U_\Xi(E = 0)$. The width Γ is indicated by the error bar when the error bar is larger than the symbol. Energy levels of the pure Coulomb potential $U_{\rm Coulomb}$ of the uniform charge distribution with a radius of $R_{\rm C} = 1.15A^{1/3}$ fm are also shown with dashed connecting lines.

coupling is smaller. Note that in the parametrization of Ref. [9], the coupling potential to the $\Sigma\Sigma$ channel is not explicitly parametrized and its effect is effectively included in the ΞN potential.

Another factor of the smallness is the spin–isospin structure. The $\Xi N \leftrightarrow \Lambda\Lambda$ conversion is possible only in the isospin $T = 0$ $^1S_0$ channel. The statistical factor $(2S + 1)(2T + 1)$ suggests that the contribution from the $T = 1$ $^1S_0$ channel is comparably suppressed, namely 1/16 in all spin–isospin combinations of the ΞN pair.

Ξ^- single-particle energies evaluated by the ILDA potential of Fig. 6 are shown in Fig. 8. The state is specified by its orbital angular momentum ℓ and the nodal quantum number n. The energies of the pure Coulomb potential of a uniform charge distribution with a radius of $R_{\rm C} = 1.15A^{1/3}$ fm are also included for comparison. The level position $e_{\rm real}$ and the width Γ of the Ξ state correspond to the complex eigenvalue of the Schrödinger equation:

Table 1. Ξ^- energies and the root-mean-square radius $\sqrt{\langle r^2\rangle}$ of the $\ell = 4$ and adjacent levels evaluated with $U_{\rm Coulomb}$ and $U_{\rm Coulomb} + U_\Xi$ in ^{56}Fe. The level shift given at the right end is $\Delta e \equiv e_{\rm C} - e_{\rm real}$. Entries for the energies $e_{\rm C}$, $e_{\rm real}$, Γ, and Δe are in keV. The unit for the root-mean-square-radius $\sqrt{\langle r^2\rangle}$ is fm.

Node	ℓ	$e_{\rm C}$	$\sqrt{\langle r^2\rangle}$	$e_{\rm real}$	Γ	$\sqrt{\langle r^2\rangle}$	Δe
0	3	−1448.94	15.3	−1727.81	83.18	10.6	278.87
0	4	−927.87	23.2	−929.66	0.20	23.1	1.78
0	5	−644.36	32.7	−644.37	0.00	32.7	0.01
1	3	−927.16	27.1	−1114.29	38.52	21.2	187.12
1	4	−644.36	37.7	−646.28	0.24	37.5	1.93
1	5	−473.41	49.9	−473.43	0.00	49.9	0.02
2	3	−643.85	41.3	−755.01	18.26	34.2	111.15
2	4	−473.40	54.5	−475.04	0.20	54.2	1.63
2	5	−362.45	69.4	−362.47	0.00	69.4	0.02
3	2	−633.61	44.5	−747.87	5.30	37.6	114.27
3	3	−473.05	57.9	−542.76	10.16	49.7	69.71
3	4	−362.45	73.7	−363.75	0.16	73.4	1.30

$$e_\Xi = e_{\rm real} + e_{\rm imag} = e_{\rm real} - i\frac{\Gamma}{2}. \tag{8}$$

The inclusion of U_Ξ appreciably lowers the Coulomb levels with the angular momentum $\ell \leq 3$. Reflecting the small imaginary part, the width of the level is at most 0.5 MeV. The level with $\ell = 4$ is the main target to experimentally detect the atomic level shift by the Ξ–^{56}Fe hypernuclear potential [4]. Table 1 tabulates energies and predicted shifts of the $\ell = 4$ and adjacent levels. These energies are not affected by the inclusion of the Ξ spin–orbit potential discussed in the preceding subsection. The smallness of the width of the $\ell = 4$ level is remarkable, though the uncertainties are kept in mind in the various stages of the present calculation.

4. Summary

Ξ hypernuclear single-particle states predicted by the Ξ–nucleus potential derived from the chiral NLO ΞN interactions with a cutoff scale of $\Lambda_{\rm c} = 550$ MeV by the Jülich–Bonn–München group [6,7] are presented and compared with those of the two sets of parametrizations based on the HAL-QCD calculations [8,9]. To learn the basic spin–isospin structure of the present ΞN interactions, ΞN phase shifts are discussed. It is also pointed out by Faddeev calculations that no ΞNN bound state is expected in every spin–isospin state. First, the Ξ states in ^{14}N are revisited. Considering the experimental observation of a probable Ξ^- p-state in ^{14}N, discussion is included about the ΞN spin–orbit interactions which are relevant to the location of the p-state. Then, the Ξ single-particle states in ^{56}Fe are calculated. In particular, the atomic level shift expected to be measured experimentally in the near future is predicted. The smallness of the imaginary part of the Ξ single-particle potential is demonstrated. The smallness is due to the small transition interaction between ΞN and $\Lambda\Lambda$, in addition to the fact that the transition to the $\Lambda\Lambda$ state is possible only in the isospin $T = 0$ ^{1}S$_0$ channel.

The parametrization of the baryon–baryon interactions in the $S = -2$ sector seems to still be in an exploratory stage due to the scarce and less-accurate experimental scattering data. Although Ξ hypernuclear data is valuable, it is difficult to deduce spin–isospin properties of the ΞN interactions by phenomenological analyses of the experimental data of Ξ states in nuclei because there are four

spin–isospin channels and various baryon-channel couplings are involved. Therefore, studies based on microscopic baryon–baryon interactions that are as reliable as possible are important. Besides the J-PARC experiments addressed in this article, studies of the p–Ξ^- interaction through the correlation function based on the ALICE femtoscopy measurements have progressed [29]. Experimental data in the near future and theoretical microscopic studies should improve our understanding of baryon–baryon interactions in strangeness sectors.

Acknowledgements

This work is supported by Japan Society for the Promotion of Science (JSPS) KAKENHI Grant No. JP19K03849. The authors thank T. Inoue for supplying them with the code of the HAL-QCD potentials in the $S = -2$ sector.

References

[1] S. H. Hayakawa et al. [J-PARC E07 Collaboration], Phys. Rev. Lett. **126**, 062501 (2021).
[2] K. Nakazawa et al., Prog. Theor. Exp. Phys. **2015**, 033D02 (2015).
[3] T. Nagae et al., AIP Conf. Proc. **2130**, 020015 (2019).
[4] K. Tanida et al. [XiX collaboration], Hyperfine Interact. **193**, 81 (2009).
[5] H. Polinder, J. Haidenbauer, and U.-G. Meißner, Phys. Lett. B **653**, 29 (2007).
[6] J. Haidenbauer, U.-G. Meißner, and S. Petschauer, Nucl. Phys. A **954**, 273 (2016).
[7] J. Haidenbauer and U.-G. Meißner, Eur. Phys. J. A **55**, 23 (2019).
[8] T. Inoue [HAL QCD Collaboration], AIP Conf. Proc. **2130**, 020002 (2019).
[9] K. Sasaki et al., Nucl. Phys. A **998**, 121737 (2020).
[10] K.-W. Li, T. Hyodo, and L.-S. Geng, Phys. Rev. C **98**, 065203 (2018).
[11] M. Kohno, Phys. Rev. C **100**, 024313 (2019).
[12] H. Garcilazo and A. Valcarce, Phys. Rev. C **93**, 034001 (2016).
[13] I. Filikhin, V. M. Suslov, and B. Vlahovic, Math. Model. Geom. **5**, 1 (2017).
[14] M. N. Nagels, Th. A. Rijken, and Y. Yamamoto, arXiv:1504.02634 [nucl-th] [Search INSPIRE].
[15] M. N. Nagels, Th. A. Rijken, and Y. Yamamoto, Phys. Rev. C **102**, 054003 (2020).
[16] J. L. Friar et al., Phys. Rev. C **42**, 1838 (1990).
[17] E. Epelbaum, W. Glöckle, and U.-G. Meißner, Nucl. Phys. A **747**, 362 (2005).
[18] K. Miyagawa and M. Kohno, Few-Body Syst **62**, 65 (2021) [arXiv:2105.11258 [nucl-th]] [Search INSPIRE].
[19] M. Yoshimoto et al., Prog. Theor. Exp. Phys. **2021**, 073D02 (2021) [arXiv:2103.08793 [nucl-ex]] [Search INSPIRE].
[20] J. Cohen and H. J. Weber, Phys. Rev. C **44**, 1181 (1991).
[21] K. Tsushima, K. Saito, J. Haidenbauer, and A. W. Thomas, Nucl. Phys. A **630**, 691 (1998).
[22] G. Chanfray and J. Margueron, Phys. Rev. C **102**, 024331 (2020).
[23] Y. Fujiwara, M. Kohno, T. Fujita, C. Nakamoto, and Y. Suzuki, Nucl. Phys. A **674**, 493 (2000).
[24] R. R. Scheerbaum, Nucl. Phys. A **257**, 77 (1976).
[25] D. Vautherin and D. M. Brink, Phys. Rev. C **3**, 626 (1972).
[26] M. Kohno, Phys. Rev. C **88**, 064005 (2013); **96**, 059903 (2017) [erratum].
[27] M. Kohno, Phys. Rev. C **88**, 064005 (2013); **96**, 059903 (2017) [erratum].
[28] D. W. L. Sprung and P. K. Banerjee, Nucl. Phys. A **168**, 273 (1971).
[29] F. Fabbietti, V. Mantovani Sarti, and O. Vázquez Doce, arXiv:2012.09806 [nucl-ex] [Search INSPIRE].